Profiling of Atmospheric Water Vapor with MIR and LASE

J. R. Wang, P. Racette, and M. E. Triesly
NASA Goddard Space Flight Center, Greenbelt, MD 20771

E. V. Browell and S. Ismail
NASA Langley Research Center, Hampton, VA 23681

L. A. Chang
Futuretech Corporation, Gaithersburg, MD 20878

Submitted to IEEE Transaction on Geosciences and Remote Sensing

February 6, 2001

Popular Summary
Profiling of Atmospheric Water Vapor with MIR and LASE

J. R. Wang, P. Racette, and M. E. Triesky
NASA Goddard Space Flight Center, Greenbelt, MD 20771

E. V. Browell and S. Ismail
NASA Langley Research Center, Hampton, VA 23681

L. A. Chang
Futuretech Corporation, Gaithersburg, MD 20878

This paper presents the first and the only simultaneous measurements water vapor by MIR (Millimeter-wave Imaging Radiometer) and LASE (Lidar Atmospheric Sounding Experiment) on board the same ER-2 aircraft. Water vapor is one of the most important constituents in the earth's atmosphere, as its spatial and temporal variations affect a wide spectrum of meteorological phenomena ranging from the formation of clouds to the development of severe storms. Its concentration, as measured in terms of relative humidity, determines the extinction coefficient of atmospheric aerosol particles and therefore visibility. These considerations point to the need for effective and frequent measurements of the atmospheric water vapor. The MIR and LASE instruments provide measurements of water vapor profiles with two markedly different techniques. LASE can give water vapor profiles with excellent vertical resolution under clear condition, while MIR can retrieve water vapor profiles with a crude vertical resolution even under a moderate cloud cover. Additionally, millimeter-wave measurements are relatively simple and provide better spatial coverage.

Profiling of Atmospheric Water Vapor with MIR and LASE

J. R. Wang[1], P. Racette[1], M. E. Triesky[1], E. V. Browell[2], S. Ismail[2], and L. A. Chang[3]

Abstract.

Concurrent measurements of atmospheric water vapor profiles were conducted over the Atlantic Ocean on September 25, 1995 with both Millimeter-wave Imaging Radiometer (MIR) and Lidar Atmospheric Sounding Experiment (LASE) on board the NASA ER-2 aircraft. LASE provides high precision measurements of profiles of both aerosol backscatter and water vapor with high vertical resolution of 60 m for aerosol backscatter and 330 m in the low-to-mid troposphere and 550 m in the upper troposphere for water vapor. LASE measurements are, therefore, an excellent resource to calibrate the capability and limitation of MIR as a water vapor profiler. Previously, the water vapor profiles retrieved from the MIR measurements have been compared with those of rawinsonde and Raman lidar observations at point locations. The frequency and extent of the comparisons made in that fashion were largely constrained by the requirement of near coincidence in time and space. The data acquired concurrently by MIR and LASE from this ER-2 aircraft flight enable the comparison of MIR-retrieved and LASE-measured moisture profiles over a long stretch of time and space. In addition, the LASE-measured profiles of aerosol backscatter provide the means to assess the impact of clouds on retrieval of water vapor profiles from the MIR measurements.

It is shown that profiles of water vapor mixing ratio retrieved from the MIR data generally conform to those measured by the LASE. Differences in the values of mixing ratio at individual altitude levels are quite often not small, however. A substantial portion of these differences is shown to be due to the poor vertical resolution inherent in the profile retrieval from the radiometric measurements. MIR water vapor profiling under cloudy conditions is also

demonstrated, and the location and height of the low-altitude clouds estimated from the retrieval process were generally consistent with those observed by the LASE. In the region of cirrus clouds where appreciable 220 GHz brightness temperature depressions occurred, retrievals from the MIR data result in the over-estimation of mixing ratio. A procedure to account for the millimeter-wave scattering by ice particles is needed in the algorithm to improve MIR water vapor profiling over the region of cirrus clouds.

---

1. Laboratory for Hydrospheric Processes, NASA Goddard Space Flight Center, Greenbelt, MD

2. NASA Langley Research Center, Hampton, Virginia

3. Futuretech Corporation, Gaithersburg, MD

1. Introduction.

Profiling of atmospheric water vapor using the strong absorption line at 183.3 GHz has been studied for nearly two decades [1-13]. Theoretically, Schaerer and Wilheit [1] explored the characteristics of this strong water vapor line by performing both forward calculations and profile retrievals over the ocean surface. The approach was extended by Wilheit [7] to retrieve water vapor profiles under both clear and cloudy conditions. Other alternative simulation studies and analyses have been performed by Rosenkranz et al.[2], Kuo et al. [11] and Muller et al. [12]. Experimentally, water vapor profiles have been retrieved using radiometric measurements by the Airborne Microwave Moisture Sounder (AMMS) in the 1980's [3-6]. AMMS is a cross-track scanning radiometer that operates at four frequencies of 90, 183.3±2, 183.3±5, and 183.3±9 GHz, and has a temperature sensitivity (ΔT) of about 4-5 K at all channels, based on 70 msec integration time [3]. Because of its limited number of channels and poor ΔT's, the AMMS radiometric measurements could not provide robust retrievals of water vapor profiles under a cloudy sky [8]. More recently, a Millimeter-wave Imaging Radiometer (MIR) was built and demonstrated to be far superior than the AMMS through a number of field experiments [9-10]. It contains six channels in the frequency range of 89-220 GHz and, with a comparable integration time of the AMMS, has ΔT's of < 1 K at all channels [14]. The radiometric measurements from this sensor have been used to retrieve water vapor profiles under cloudy conditions with reasonable success [10]. Burns et al.[13] have also examined the effects of precipitation and cloud ice on these water vapor channels using measurements from the SSM/T-2 (Special Sensor Microwave/Temperature-2) on board the DMSP (Defense Meteorological Satellite Program) F-11 satellite. These theoretical and experimental efforts provide an effective demonstration of the capability and limitation of using the 183.3 GHz line for water vapor profiling.

The experimental results of water vapor profiling derived from the AMMS and MIR measurements were routinely compared with nearly concurrent (within ±3 hours) rawinsonde observations at some selected locations [3, 6, 9]. A comparison of water vapor profiles retrieved from the MIR measurements was also made with ground-based Raman lidar observations at NASA's Wallops Flight Facility (WFF), Wallops Island, Virginia during the Convection and Atmospheric Moisture Experiment (CAMEX) of July 20-August 6, 1993 [9]. Reasonable agreements were found between the profiles retrieved from these AMMS and MIR measurements and those measured at the ground locations. However, these comparisons were limited to single locations and there has been no validation of the profiles retrieved from the measurements of these millimeter-wave sounders over an extended region. During September 1995, MIR and LASE (Lidar Atmospheric Sensing Experiment) were on board the NASA ER-2 aircraft during a number of flights both over land and ocean areas in the eastern U.S. LASE measures both aerosol backscatter and water vapor mixing ratio with high accuracy and vertical resolution. The LASE-measured values of mixing ratio were compared with those measured concurrently by the ground-base Raman Lidar and rawinsondes at WFF and an excellent agreement was found among the three different approaches [15]. These flights provided the first opportunity to validate the water vapor profiling from the MIR radiometric measurements over an extended region.

In the following we present and discuss the results of these concurrent LASE and MIR measurements. The scenario of an LASE and MIR inter-comparison flight and the characteristics of LASE and MIR are described in Section 2. Time variations of LASE-measured aerosol backscatter and water vapor profiles, as well as the MIR-measured brightness temperatures are presented in Section 3. Retrievals of water vapor profiles from the MIR measurements and

comparison of these profiles with those from the LASE measurements are given in Section 4. The characteristics and limitation in vertical resolution of the water vapor profiles retrieved from the MIR measurements are discussed in Section 5. Finally, the main features derived from the analysis of these concurrent MIR and LASE measurements are summarized in Section 6.

2. The Measurements.

The measurements presented in the following sections were made concurrently by the MIR and LASE on board the NASA ER-2 aircraft on September 25, 1995 over the ocean areas east of the Carolinas. The aircraft was stationed at NASA Goddard Space Flight Center's (GSFC) Wallops Flight Facility (WFF), Wallops Island, Virginia, during September 1995 for the LASE Validation Experiment. The flight on September 25 was one of few that the MIR data were not corrupted by LASE aircraft-to-ground telemetry signals. The ER-2 aircraft took off from the WFF around 1700 UTC and spent the first three hours of the flight over land that is not of interest to this paper. The latter part of the flight beginning around 2020 UTC was over the ocean areas where water vapor profiles could be readily derived from the MIR radiometric measurements [9-10]. LASE provided water vapor profiles with high vertical resolution both over land and water surfaces. Figure 1 shows a sketch of the flight path of the ER-2 aircraft for this latter part of the flight. A few tick marks on the flight track give the UTC times of the aircraft locations. The concurrent MIR and LASE measurements along five straight line segments, indicated by L1, L2, L3, L4, and L5, are analyzed and presented in the following sections. The L2, L3 and L4 legs give the repeated measurements over the same region. The oceanic regions covered by the flight are mostly clear; patches of high-altitude cirrus clouds and low-altitude liquid clouds are also present in some segments of these flight lines.

The MIR is a six-channel (89, 150, 183.3±1, 183.3±3, 183.3±7, and 220 GHz) cross-track scanning total-power radiometer mounted on the right-wing superpod of the ER-2 aircraft. The sensor has a 3-dB beamwidth of about 3.5° at all frequency channels and covers an angular swath of ±50° with respect to nadir. In every scan cycle (about 2.9 sec in normal operational mode), it views two external calibration targets; one of them is heated to a temperature of approximately 330 K and another remains at the ambient temperature that, at the cruising altitude of the ER-2 aircraft, is about 240 K. The temperatures of these calibration targets are closely monitored to within ±0.1 K. The temperature sensitivity (ΔT) for all six channels is about 0.5 K based on 70 msec integration time. The calibration accuracy is better than ±2 K in the brightness temperature ($T_b(\nu)$, ν is frequency) range of 240-300 K. At $T_b(\nu)$ below 240 K, the measurement accuracy is somewhat uncertain; based on the calibration studies in the laboratory, the accuracy near the liquid nitrogen temperature of 77 K is estimated to be ±3 K [14].

The Lidar Atmospheric Sensing Experiment (LASE) system was developed at the NASA Langley Research Center to measure atmospheric water vapor and aerosols profile, and cloud distributions from aircraft [15-16]. LASE is a compact and highly engineered Differential Absorption Lidar (DIAL) system that has demonstrated autonomous operation from the high-altitude ER-2 aircraft as a precursor to a space-borne DIAL system. The laser system consists of a double-pulsed Ti:sapphire laser that operates in the 815-nm absorption band of water vapor and is pumped by a frequency doubled Nd:YAG laser. The double pulsing is needed to generate the 'on' and 'off' line pair needed for the DIAL water vapor measurements. The wavelength of the Ti:sapphire laser is controlled by injection seeding with a diode laser that is frequency locked to a water vapor absorption line using an absorption cell. LASE operates locked to peak of a strong water vapor absorption line profile and electronically tunes to any spectral position on the

absorption line (side-line position). This permits the selection of an absorption cross-section that is optimum over a range of water vapor concentrations. LASE is capable of transmitting a combination of the wavelength pairs that together permit an optimum profiling of water vapor over the entire troposphere. The detector system uses silicon avalanche photo diodes and multiple digitizers to cover a large signal dynamic range (10^6), and the signal processor system was designed to be relatively insensitive to rapid changes in signal levels. The capability of LASE for profiling tropospheric water vapor and aerosol profiles, and cloud distributions was demonstrated during the LASE Validation Experiment [16] that was conducted during September 9-26, 1995 at NASA Wallops Flight Facility in conjunction with the CAMEX-2. During the L1 to L5 segments (Figure 1) of the flight on September 25, 1995, LASE was operated, for the first time, in a two line-pair combination to measure water vapor from the ground to the tropopause region. In addition to water vapor profiles, aerosol scattering ratios and cloud distributions were measured.

To facilitate discussion of the observed variations of brightness temperatures in the next section, the weighting functions (W(ν, h), h being the altitude) at six MIR frequencies between 89-220 GHz are calculated and displayed in Figure 2 for two hypothetical atmospheric conditions: one extremely moist at 100% uniform relative humidity (RH) and another rather dry at 30% uniform RH. A temperature profile generated by ECMWF (European Center for Medium-range Weather Forecast) in the region of the aircraft flight was assumed in the derivation of these functions. The maximum of W(ν, h)'s for the three 183-GHz channels shifts to higher altitudes as RH changes from 30% to 100%. At 30% RH, surface emission contributes significantly to the $T_b(\nu)$'s at all three window channels (89,150 and 220 GHz); there is a small surface contribution at 183.3±7 GHz too. Assuming a sea surface temperature of 300 K, the

calculated $T_b(\nu)$ values corresponding to these W(v h)'s are 208, 257, 249, 265, 280, and 280 K for ν = 89, 150, 183.3±1, 183.3±3, 183.3±7, and 220 GHz, in sequential order. At 100% RH, these values become 262, 282, 236, 253, 267, and 276 K. There is an increase in both $T_b(89)$ and $T_b(150)$ and a decrease in $T_b(220)$ as the atmosphere changes from dry to moist condition. A reversal in $T_b(\nu)$ at 150 and 220 GHz is also observed; at 30% RH, $T_b(150) < T_b(220)$, and at 100% RH, $T_b(150) > T_b(220)$. At all three 183.3 GHz channels, $T_b(\nu)$ values decrease as RH changes from 30% to 100%. These trends are observed by the MIR measurements described in the next section.

3. Results.

Figure 3, (a) and (b) respectively, shows the profiles of aerosol backscatter (in terms of relative backscattering β) and water vapor mixing ratio (ρ) measured by the LASE over a 20-minute period between 2033 and 2053 UTC, covering the middle portion of the flight leg L1. Both parameters are expressed in gray scale indicated on the right side of the figure. For aerosol backscatter in Figure 3(a), the totally black pixels represent two different scenarios: either β is $\geq$ 420 or dense clouds at higher altitudes totally attenuate the LASE signal returns below them. Three conspicuous examples of the latter are indicated by the arrows A, B, and C in Figure 3(a) where the regions of LASE signal attenuation extend from the surface to 2-3 km altitudes. At the locations of B and C, the cloud tops occur around 5 km, while at the location of A, about 3 km. These clouds are small liquid drops that absorb and emit radiation at MIR frequencies as described below. In between A and B there are patches of moderately dense ice clouds in the altitude range of 7-11 km. The presence of liquid and ice clouds affects the LASE measurements of ρ profiles displayed in Figure 3(b). In the regions of liquid clouds, LASE could not provide

measurements of ρ at altitudes below ~ 3 km. LASE data over the altitude region 4.5-7.0 km have been edited to avoid the bias due to saturation effects over the patches of ice clouds.

The LASE measurements of ρ cover an effective altitude range of 0.6-16 km; as a consequence, there is a gap between the surface and the 0.6 km altitude in Figure 3(b). In addition to the four regions associated with the dense clouds discussed above, there are a few places where no ρ measurements are made below ~ 2 km. These are presumably caused by some low-level liquid clouds or dense aerosol shown in Figure 3(a). Besides these minor deficiencies, the LASE measurements generally provide ρ profiles with high vertical resolution that compare well with those measured by rawinsondes and ground-based Raman lidar at WFF [16]. Notice that, from the beginning of Figure 3(b) at 2033 UTC to the end at 2053 UTC, there is a general increase in ρ. This can be seen from the gradual change in gray scale of the pixels between the altitudes of 2-6 km.

The corresponding brightness temperature variations measured by the MIR over the same time period are shown in Figure 4. The resolution of $T_b(89)$ along the vertical axis is reduced by a factor 2 relative to that at other frequencies to allow for large variations caused by the presence of cloud covers. The peaks in the $T_b(89)$ curve are caused by the low-altitude liquid clouds. The three pronounced maxima in $T_b(89)$ denoted by arrows A, B, and C occur at the same locations of low-altitude clouds observed by the LASE displayed in Figure 3. The $T_b(89)$ increases as a result of increased emission from the liquid water. The values of $T_b(150)$ and $T_b(220)$ are generally in the 280-285 K range, implying that in W(v,h)'s for these channels peak in the altitude range of 1-4 km. The radiation observed by these channels predominantly originates from the same lower atmosphere where the low-altitude liquid clouds are observed by the LASE. As a consequence, the low sensitivity of these channels to the low-altitude clouds is reflected in

the small variations in both $T_b(150)$ and $T_b(220)$. At the locations of B and C, the absorption and emission by liquid water near the cloud-top freezing-level temperature apparently lower both $T_b(150)$ and $T_b(220)$. The 183.3±7 GHz channel also experiences this effect, albeit to a smaller extent; in the absence of clouds, W(183.3±7, h) may peak around 4-km altitude in the neighborhood of B and C.

Besides features associated with these low-altitude clouds, the values of $T_b(89)$ generally show a gradual increase from 2033 to 2053 UTC. This is accompanied by the gradual decrease in both $T_b(183.3\pm7)$ and $T_b(183.3\pm3)$ over the same period. From the curves of Figure 2, this indicates a gradual enhancement of column water vapor from the location at 2033 UTC to that at 2053 UTC. The absence of $T_b(183.3\pm1)$ decrease suggests that the enhancement of water vapor from 2033 to 2053 UTC occur mostly in the middle troposphere, consistent with the LASE observations in Figure 3. The $T_b(220)$ also shows some gradual decrease from 2033 to 2053 UTC, implying that W(v, h) shifts slightly to a higher altitude and the surface contribution to $T_b(220)$ is minimal. A slight initial increase followed by a very slight decrease in $T_b(150)$ suggests that the maximum of W(150, h) occurs near the surface. Notice that there is a broad brightness depression for all three 183.3 GHz channels around 2048 UTC, which apparently is related to the presence of ice clouds near 9-km altitude (Figure 3). This is likely caused by the enhancement of water vapor in the region of ice clouds. Scattering of radiation by ice clouds also gives brightness depression [17-20], but the minimal depression at the higher frequency channel (i.e., 220 GHz) rules out this process as the dominant effect. Similar observations on water vapor variations are made when comparing LASE and MIR measurements from flight leg L5.

The measurements over the region covered by L2, L3, and L4 compare differently. Figure 5 shows the LASE-measured β and ρ for the two consecutive passes L2 (flight from southwest to

northeast) and L3 (flight from northeast to southwest) over the region. It is evident from Figure 5a that the atmosphere is mostly clear on the southwest portion of the flight path. On the northeast portion of the flight, the region is covered with dense cirrus clouds at altitudes ≥ 9 km; LASE signals are totally attenuated below the base of these clouds, and the measured profiles of ρ are limited to the region above the cloud base. Over the region of clear sky, the LASE-measurements show the vertical distribution of water vapor in great detail. Notice that the structures of ρ variations between L2 and L3 are nearly symmetric in this region, indicating repeatability and reliability of the LASE measurements.

Figure 6 shows the variations of the corresponding MIR-measured $T_b(\nu)$'s from the same L2 and L3 passes. The values of $T_b(89)$ remain fairly constant for both passes over the region. The slightly higher values at a few locations are associated with low-level clouds observable from Figure 5a. The high-altitude dense cirrus clouds appear to cause some depressions in $T_b(\nu)$'s at $\nu \geq 150$ GHz, but do not show much effect on the 89 GHz channel. At the largest depressions near 2155 UTC, $T_b(\nu)$'s decrease by ~2 K, ~4 K, and ~8 K at ν = 150, 183.3±7, and 220 GHz respectively. This strong frequency dependence of brightness depressions is consistent with the observations of cirrus clouds over northern Oklahoma and arctic region reported by Wang et al.[17-18]. There is some enhancement in $T_b(89)$ just beyond 2155 UTC. This is related to the low-level clouds in the 1-1.5 km altitude range detected by the LASE and shown in Figure 5a.

4. Comparison of Water Vapor Profiles.

The algorithm used for the retrieval of ρ's from the MIR radiometric measurements has been reported previously [9-10]. It is capable of retrieving profiles of ρ under either clear sky or moderate, low-level cloud cover through iterative process [10]; the effect of millimeter-wave

scattering by the cirrus clouds [17-20] is not considered in the retrieval. Besides the six channels of MIR-measured $T_b(\nu)$ values, atmospheric temperature profiles and sea surface temperature (SST) are needed in the retrieval; these are obtained from the ECMWF (European Center for Medium-range Weather Forecast) derived products near the time and region of the measurements. A calm water surface is assumed for simplicity; the impact of the effect of wind-roughened ocean surface on the surface emissivity and, therefore, on water vapor profiling is shown to be small when surface wind speed is $\leq$ 10 m/s [9]. The revised atmospheric millimeter-wave propagation model of Liebe [21] and Liebe et al. [22] is used for the calculations of absorption coefficients by the atmospheric gases at the MIR frequencies. In each iteration, the $T_b(\nu)$ values at the six frequency channels of the MIR are calculated from the estimated ρ profile and compared with the measured ones. The quality of this comparison is expressed in terms of the root-mean-square of the differences between the calculated and measured $T_b(\nu)$ values, δT_b, as

$$\delta T_b = \{\frac{1}{n-1}\sum_{\nu=1}^{n}[T_{bc}(\nu) - T_{bm}(\nu)]^2\}^{1/2} \qquad (1)$$

where the subscript m and c, respectively, refer to the measured and calculated $T_b(\nu)$ values. When δT_b is less than or equal to a specified quantity ε (which is set equal to 1 K, conforming to the accuracy of the MIR measurements) at any iteration, the retrieval is considered convergent and the resultant ρ profile adequate for the measured $T_b(\nu)$ values. If $\delta T_b > \varepsilon$, a new ρ profile is estimated and the new δT_b computed through another iteration. Convergence is normally achieved within 4-5 iterations. The retrieval is stopped and results output when the number of iterations reach a pre-determined value (10 in the present case); in these cases the resultant δT_b is

$\geq$ 1 K. The ρ's are retrieved at six altitudes of 0.25, 1.25, 2.25, 4.75, 7.25 and 10.25 km from six channels of the MIR measurements.

Figure 7 shows the results of the retrieval for the same time interval displayed in Figures 3 and 4: (a) profiles of ρ expressed in terms of gray scale, (b) estimated total cloud liquid water and cloud top, and (c) total precipitable water (TPW) and δT_b. Here the TPW values are estimated by simply integrating the ρ profiles in Figure 7a, and cloud liquid water includes estimation at all levels below the cloud top. The retrieval at the maximum height of 10.25 km is reflected from the boundary of ρ profiles in Figure 7a. A gradual enhancement of ρ from 2033 to 2053 UTC can be seen from Figure 7a at altitudes $\leq$ 7 km; this trend is clearly displayed in Figure 7c as TPW increases from ~ 4 g/cm^2 to $\geq$ 5 g/cm^2 over the same period. Higher ρ values are generally associated with areas where low-altitude liquid clouds are observed by the LASE (Figure 3a). The cloud tops displayed in Figure 7b correspond closely with the ones measured by LASE aerosol backscatter in Figure 3a. The area covered by the cirrus clouds (between arrows A and B in Figure 3a) appears totally clear to MIR. No cloud liquid water is estimated in this area; only some enhancement in ρ appears in the altitudes $\geq$ 4 km. For the two cloud cells (B and C in Figure 3a) near 2051 UTC, where LASE-measured cloud tops are about 5 km (Figure 3a) and $T_b(89) \geq 270$ K (Figure 4), the retrievals of ρ profiles face some uncertainties; low ρ values are retrieved at altitudes below 3 km and $\delta T_b \cong$ 2-3 K. These belong to the class of dense liquid clouds for which the retrievals of ρ profiles from the MIR measurements become more uncertain [10]. For the rest of the 20-minute interval, δT_b's range between < 1 K to ~2 K.

Figure 8 compares the MIR retrieved ρ profiles with those measured by the LASE at four selected times from the same 20-minute interval. Plots a and c are from the clear areas and plots

b and d, from the two cloud cells B and C (Figure 4). In these plots, the solid curves show the LASE-measured ρ profiles and the open circles, the MIR-retrieved ρ values at six different altitudes. The LASE-measured cloud tops are indicated by the horizontal line segments with downward arrows in plots b and d. For plots a and c, the MIR-retrieved ρ values give generally smooth profiles that decrease monotonically with altitudes. These profiles compare favorably with those measured by the LASE. Because of poor vertical resolution in the MIR-retrieved profiles, appreciable difference may exist in the ρ values measured by the two sensors at a given altitude h. For example, at $h < 3$ km, the differences between the MIR-retrieved and LASE-measured ρ's from these plots can be as large 2 g/kg. Plots b and d shows that, at altitudes greater than the cloud top of ~5 km, the MIR-retrieve and LASE-measured ρ's compare favorably. LASE could not make ρ measurements at $h \leq 2.5$ km, and the MIR-retrieved ρ values are not reliable for these dense clouds, as noted in the discussion of Figure 7a.

A comparison between MIR-retrieved (solid curves) and LASE-measured (open circles) ρ values at five different h's over the entire 20-minute interval is shown in Figure 9. At $h = 1.25$ km, there are a number of places with missing LASE data due to the attenuation of low-altitude clouds. Data gap in LASE-measured ρ's also occurs at $h = 7.25$ km and $h = 2.75$ below the intense cirrus clouds observed around 2048 UTC (see Figure 3). Some of the LASE data points at all h's in the immediate neighborhood of these gaps could be unreliable. For the three levels at $h \leq 4.75$ km, there is a very good agreement between the LASE-measured and MIR-retrieved ρ's; the differences in ρ's measured by the two sensors are generally ≤ 2 g/kg. At $h = 7.25$ km and $h = 10.25$ km where ρ values are small, the fractional differences in the measurements from the two sensor appear more appreciable (small when plotted in the scale of Figure 8). Some of these

differences are intrinsic in the profiling of ρ from the MIR measurements to be discussed in the next section.

A similar comparison between the LASE-measured and MIR-retrieved ρ's from the flight legs L2 and L3 is displayed in Figure 10. The region under intense cirrus clouds (see Figure 5) is in the middle portion of the figure and ρ is not measured by the LASE at $h \leq 7.25$ km. At h = 10.25 km, the ρ values from both sensors agree very well except in the areas of cirrus clouds. For an interval of about 2-3 minutes in the cirrus cloud area, around ~2139 UTC from L2 and ~2152 UTC from L3, both LASE and MIR detect an enhancement of ρ and the ρ values from both sensors agree reasonably well; in the other areas the MIR-retrieved values are generally higher. At h = 2.75, 4.75, and 7.25 km, the MIR-retrieved ρ's in the areas of cirrus are also higher than those in the areas of clear sky. While the ρ's are expected to be enhanced in the regions of cirrus clouds, the MIR-estimated values could be on the high side, because our retrieval algorithm does not deal with scattering of radiation by ice particles; i.e., the brightness temperature depression caused by ice-particle scattering is treated the same as that caused by water vapor enhancement.

5. Discussion.

It was pointed out in the previous section that the ρ profiles retrieved by radiometric measurements from a passive sensor such as MIR are intrinsically of poor vertical resolution. Consequently, these profiles provide a general trend of altitude variations of ρ's like those displayed by plots (a) and (c) in Figure 8. A comparison, at a given altitude, of ρ's derived from the MIR measurements with those measured by the LASE with a fine vertical resolution would sometime result in appreciable differences. To illustrate this effect more explicitly, $T_b(\nu)$'s at the

MIR frequencies have been calculated using the LASE-measured ρ profiles and the same temperature profiles generated by the ECMWF and used in the retrieval presented in the previous section. Since the LASE measurements end at h = 0.6 km, the ρ's below that altitude are extrapolated before the forward calculations of $T_b(v)$'s are performed. The calculated $T_b(v)$'s are then input to the retrieval algorithm for derivation of ρ profiles. The retrieved ρ values at four different h's (represented by +) are compared with the original ones (open circles) in Figure 11 for flight leg L1. Notice that there are a number of places where there are no retrieved ρ's. These are places where there are no LASE measurements below 1 km; these locations are excluded from the calculations and retrievals.

Figure 11 shows that the retrieved ρ's are quite often not close to the ones originally measured by the LASE. At h = 2.75 km and h = 4.75 km, the differences between the retrieved and measured ρ's could differ by as much as 2 g/kg, comparable to those resulting from the comparison of MIR-retrieved and LASE-measured ρ's shown in Figure 9. The measured ρ's generally show more temporal variations than the retrieved ρ's. At h = 7.25 km the retrieved ρ's for the period before 2045 UTC are lower than the measured ones. At h = 10.25 km the retrieved ρ's are slightly higher than the measured ones over the same period. Comparing these results with those displayed in Figure 9 suggests that part of the differences between the LASE-measured and MIR-retrieved ρ's in that figure is inherent in the retrieval process, and a better agreement is expected between the MIR-retrieved and LASE-retrieved ρ's. This is more clearly shown in Figure 12 where the MIR-retrieved (solid curves) and LASE-retrieved (open circles) ρ's are compared for the portions of L1, L2, and L3 in which the LASE-retrieved ρ's are most populated. In reference to Figure 9 for L1, an improved agreement between the MIR- and LASE-

retrieved ρ's at all four altitude levels is quite evident in Figure 12. For L2 and L3 the agreement between the MIR- and LASE-retrieved ρ's is excellent at both h = 2.75 km and h = 4.75 km. At higher altitudes of 7.25 km and 10.25 km, the LASE-retrieved ρ's are mostly smaller than the MIR-retrieved ρ's. Comparing to the corresponding data in Figure 10, the agreement between the MIR- and LASE-retrieved ρ's is slightly better at h = 7.25 km and slightly worse at h = 10.25 km. These differences between the MIR- and LASE-retrieved ρ's in Figure 12 could be attributed to the accuracy of the measurements and the deficiency in the retrieval algorithm.

It was pointed out in Section 4 that the algorithm used to retrieve ρ profiles from the MIR radiometric measurements deals only with the absorption by water vapor and liquid clouds; scattering of millimeter-wave radiation by cirrus (ice) clouds [17-20] is totally ignored by the algorithm. The effect of scattering by cirrus clouds is reflected in the depression of $T_b(\nu)$'s at the MIR frequencies [17-18], which is similar to that caused by the enhancement of atmospheric water vapor discussed in Section 2. Thus, the high MIR-retrieved ρ values at h = 7.25 and 10.25 km in L2 and L3 in Figure 12 could be the results of $T_b(\nu)$ depressions caused by cirrus clouds. To obtain accurate ρ profiles from the MIR measurements over a region of cirrus clouds, the retrieval algorithm will have to be upgraded to include the effect of millimeter-wave scattering by the ice particles.

Using the LASE measurements as a standard by which to compare ρ profiles, the errors in the MIR-retrieved ρ profiles, due to the uncertainties in the MIR measurements and ECMWF-supplied temperature profiles, are approximately assessed. This is accomplished through calculations of the standard deviations ($\Delta\rho_m(h)$) of the differences between the concurrent MIR-retrieved and LASE-measured ρ(h)'s, at the five different h's of 1.25, 2.75, 4.75, 7.25, and 10.25

km. The results are given in the first column of Table 1, where the first number before the ± sign is the bias (average) of the $\rho(h)$ differences at a given h. Similar calculations are also made for the $\Delta\rho_l(h)$'s between the LASE-retrieved and LASE-measured $\rho(h)$'s, and the results are shown in the second column of the same table; these approximately give the errors that are inherent in the retrieval process. In third column of the table the averages ($\rho_l(h)$) and standard deviations of $\rho(h)$'s measured by the LASE over all five flight segments are given. Finally, the averages ($\rho_c(h)$) and standard deviations of $\rho(h)$'s derived from the rawinsonde data from Charleston, South Carolina (32.9°N, 80.03°W) over a 3-month period of April-June 1996) are also entered in the last column of the table for reference and comparison. Notice that $\rho_c(h)$'s are generally much smaller, but exhibit larger variations at low h, than $\rho_l(h)$'s. Some biases are present in the $\Delta\rho_l(h)$'s, although they are small compared to the typical $\rho_l(h)$ values of 6.9, 3.32, 1.0, and 0.28 g/kg at h = 2.75, 4.75, 7.25, and 10.25 km respectively.

A comparison of $\Delta\rho_m(h)$'s and $\Delta\rho_l(h)$'s suggests that intrinsic errors resulting from the retrieval process account for a substantial portion of the errors in MIR water vapor profiling. These intrinsic errors are mainly due to the poor vertical resolution inherent in the radiometric measurements (in contrast to the active measurements provided by the LASE). For $h \geq 2.75$ km, both $\Delta\rho_m(h)$'s and $\Delta\rho_l(h)$'s are smaller than the standard deviations of $\rho_l(h)$'s, implying that the ρ profiles derived from the MIR measurements could provide valuable information on the variation of the moisture field. At h = 1.25 km, $\Delta\rho_m(h)$ is only slightly smaller than the standard deviation of $\rho_l(h)$; this implies that $\rho(h)$'s derived from the MIR measurements provide limited information on the variation of moisture field at low-altitude levels. However, the variations of $\rho_l(h)$'s in Table 1, measured by the LASE over a time interval of about 3 hours only, are limited to a region

confined by the longitude and latitude ranges of 8° by 6°. Over a longer time interval and/or a larger spatial scale, ρ(h)'s are expected to display a much larger variation, like the ones shown in the $\rho_c(h)$ column at $h \leq 2.75$. The MIR measurements would provide valuable ρ profiles under such circumstances.

Table 1. Biases and standard deviations of the differences between the retrieved and measured water vapor mixing ratios.

Height	$\Delta\rho_m(h)$	$\Delta\rho_l(h)$	$\rho_l(h)$	$\rho_c(h)$
1.25	-0.35±0.98		13.66±1.17	8.00±3.57
2.75	-0.13±0.84	-0.05±0.95	6.90±2.11	3.96±2.37
4.75	0.37±0.95	0.12±0.57	3.32±1.88	1.64±1.12
7.25	0.22±0.42	0.03±0.16	1.00±0.72	0.49±0.38
10.25	0.04±0.06	0.00±0.02	0.28±0.09	0.10±0.07

6. Conclusions.

Measurements of water vapor profiles were made concurrently with LASE and MIR on board the NASA ER-2 aircraft over the Atlantic ocean on September 25, 1995. The LASE measured profiles have a vertical resolution of 330 to 550 m, depending on altitudes, and, therefore, serve as an excellent standard with which the lower-resolution profiles retrieved from the MIR measurements can be compared. Previously, the water vapor profiles obtained from the MIR measurements could only be compared with those measured by dropsondes from a different aircraft or by the ground-based Raman lidar and rawinsondes [9,10]. The requirement of the approximate coincidence in time and location of these measurements essentially limited the comparison to a few selected cases. The 3-hour flight of LASE and MIR described above, on the other hand, provides about 180 independent and concurrent measurements over the ocean area that includes both clear and cloudy conditions. The combined LASE and MIR data set serves as

an extremely valuable means to analyze and evaluate the capability and limitation of millimeter-wave remote sensing to profile water vapor. There is a deficiency in this data set: it is obtained within a short time over a small region and, as a consequence, the range of observed variation in the moisture field of the atmosphere is rather limited for the analysis.

The comparison of the MIR-retrieved profiles of water vapor mixing ratio with those measured by LASE leads to the following conclusions. For one thing, the MIR-retrieved profiles generally tracked well with those measured by the LASE, although they could not provide the fine structure reflecting the rapid changes of moisture with altitude that wss observed by LASE. At individual altitude levels, the differences in the mixing ratios retrieved by the MIR and measured by LASE are not small. A substantial portion of these differences was caused by the poor vertical resolution of the retrieved profiles that is inherent in the inversion process. The standard deviation of these differences was found to be appreciably smaller than that of climatological variations. Therefore, radiometric measurements at the MIR frequencies can provide water vapor profiles that are useful in studying the large-scale changes in the water vapor fields of the atmosphere.

Next, it was shown that MIR could profile atmospheric water vapor over a region with low-altitude moderate cloud cover. There is a close association between the locations where low-level clouds are detected by LASE and the locations where the cloud liquid water were also required for input to the algorithm to bring about a convergent retrieval of water vapor profiles from the MIR measurements. The cloud tops predicted by the retrieval algorithm appear to be closely related to those observed by the LASE. The retrieval experiences some difficulty in areas of dense clouds where the measured 89 GHz brightness temperatures are > 270 K (Figure 4). The retrievals for these areas result in low values of mixing ratio at altitudes below cloud tops,

require cloud liquid water in excess of 0.4 kg/m^2, and are associated with poor convergent criteria ($\Delta T_b \cong$ 2-3 K) (see Figure 5).

Finally, in the region of dense cirrus clouds where the depressions in 220 GHz brightness temperatures are clearly observed, the effect of millimeter-wave scattering by ice particles has to be taken into account in MIR water vapor profiling. The algorithm used to retrieve water vapor profiles from the MIR measurements, as discussed above, does not currently incorporate such a procedure. Consequently, the retrieved values of mixing ratio in the region of cirrus appear to be over-estimated when compared to those measured by the LASE. To correct this deficiency in water vapor profiling over the region of dense cirrus clouds from millimeter-wave radiometry, it will be essential to include a procedure in the retrieval algorithm to account for the scattering by ice particles.

Acknowledgements. The research conducted with MIR was supported by Dr. Ramesh Kakar, the Mesoscale Atmospheric Dynamics Program, NASA Headquarters. The LASE Validation Field Experiment was supported by Drs. James Dodge and Robert Harris of the Earth Science Enterprise, Science Division, NASA Headquarters.

References.

[1] G. Schaerer and T. T. Wilheit, "A passive microwave technique for profiling atmospheric water vapor," Radio Sci., 14, 371-375, 1979.

[2] P. W. Rosenkranz, M. J. Komichak, and D. H. Staelin, "A method for estimation of atmospheric water vapor profiles by microwave radiometer," J. Appl. Meteor., 21, 1364-1370, 1982.

[3] J. R. Wang, J. L. King, T. T. Wilheit, G. Szejwach, L. H. Gesell, R. A. Nieman, d. S. Niver, B. M. Krupp, and J. A. Gagliano, "Profiling atmospheric water vapor by microwave radiometry," J. Climate Appl. Meteor., 22, 779-788, 1983.

[4] R. K. Kakar, "Retrieval of clear sky moisture profiles using the 183 GHz water vaapor line," J. Climate Appl. Meteor., 22, 1282-1289, 1983.

[5] R. K. Kakar and B. H. Lambrigtsen, "A statistical correlation method for the retrieval of atmospheric moisture profiles by microwave radiometry," J. Climate Appl. Meteor., 23, 1110-1114, 1984.

[6] R. Lutz, T. T. Wilheit, J. R. Wang, and R. K. Kakar, "Retrieval of atmospheric water vapor profiles using radiometric measurements near 183 and 90 GHz," IEEE Trans. Geosci. Remote Sens., GE-29(4), 602-609, 1991.

[7] T. T. Wilheit, "An algorithm for retrieving water vapor profiles in clear and cloudy atmospheres from 183 GHz radiometric measurements: Simulation studies," J. Appl. Meteor., 29, 508-515, 1990.

[8] J. R. Wang, W. C. Boncyk, and A. K. Sharma, "Water vapor profiling over ocean surface from airborne 90 and 183 GHz radiometric measurements under clear and cloudy conditions," IEEE Trans. Geosci. Remote Sens., 31(4), 853-859, 1993.

[9] J. R. Wang, S. H. Melfi, P. Racette, D. N. Whiteman, L. A. Chang, R. A. Ferrare, K. D. Evans, and F. J. Schmidlin, "Simultaneous measurements of atmospheric water vapor with MIR, Raman lidar, and rawinsondes," J. Appl. Meteor., 34(7), 1595-1607, 1995.

[10] J. R. Wang, J. D. Spinhirne, P. Racette, L. A.Chang, and W. Hart, "The effect of clouds on water vapor profiling from the millimeter-wave radiometric measurements," J. Appl. Meteor., 36(9), 1232-1244, 1997.

[11] C. C. Kuo, D. H. Staelin, and P. W. Rosenkranz, "Statistical iterative scheme for estimating atmospheric relative humidity profiles," IEEE Trans. Geosci. Remote Sens., 32, 254-260,1994.

[12] B. M. Muller, H. E. Fuelberg, and X. Xiang, "Simulations of of the effects of water vapor, cloud liquid water, and ice on AMSU moisture channels brightness temperatures," J. Appl. Meteor., 33, 1133-1154, 1994.

[13] B. A. Burns, X. Wu, and G. R. Diak, "Effects of precipitation and cloud ice on brightness temperatures in AMSU moisture channels," IEEE Trans. Geosci. Remote Sens., 35(6), 1429-1437, 1997.

[14] P. Racette, R. F. Adler, J. R. Wang, A. J. Gasiewski, D. M. Jackson, and D. S. Zacharias, "Millimeter-wave imaging radiometer for cloud, precipitation, and atmospheric water vapor studies," J. Atmos. Ocean. Technol., 13, 610-619, 1996.

[15] A. S. Moore, K. E. Brown, W. M. Hall, J. C. Barnes, W. C. Edwards et al., development of lidar Atmospheric Sensing Experiment (LASE)- an advanced Airborne DIAL Instrument, in *Advances in Atmospheric Remote Sensing With Lidar*, A. Ansman, R. Neuber, P. Rairoux, and U. Wandinger (Eds.), Springer, pp281-288, 1997.

[16] E. V. Browell, S. Ismail, W. M. Hall, A. S. Moore, S. A. Kooi et al., LASE Validation Experiment, in *Advances in Atmospheric Remote Sensing With Lidar*, A. Ansman, R. Neuber, P. Rairoux, and U. Wandinger (Eds.), Springer, pp 289-295, 1997.

[17] J. R. Wang, J. D. Spinhirne, P. Racette, K. F. Evans, and W. D. Hart, "Observations of cirrus clouds with airborne MIR, CLS, and MAS," Geophy. Res. Letters, 25(8), 1145-1148, 1998.

[18] J. R. Wang, G. Liu, J. D. Spinhirne, P. Racette, and W. D. Hart, "Observations and retrievals of cirrus cloud parameters using multichannel millimeter-wave radiometric measurements," J. Geophys. Res., inpress, 2000.

[19] K. F. Evans and G. L. Stephens, "Microwave radiative transfer through clouds composed of realistically shaped ice crystals. Part II: Remote sensing of ice clouds," J. Atmos. Sci., 52(11), 2058-2072, 1995.

[20] K. F. Evans, S. J. Walter, A. J. Heymsfield, and M. N. Deeter, "Modeling of submillimeter passive remote sensing of cirrus clouds," J. Appl. Meteorology, 37, 184-205, 1998.

[21]. H. J. Liebe, "MPM - An atmospheric millimeter-wave propagation model," Int. J. Infrared Millimeter Waves, 10(6), 631-650, 1989.

[22] H. J. Liebe, G. A. Hufford, and T. Manabe, "A model for the complex permittivity of water at frequencies below 1 THz," Int. J. Infrared Millimeter Waves, 12(7), 659-675, 1991.

Figure Captions.

Figure 1. A sketch showing the path of the ER-2 aircraft flight over the Atlantic Ocean on September 25, 1995. Five straight line segments are denoted by L1, L2, L3, L4, and L5. L2, L3, and L4 are repeated passes over the same region.

Figure 2. Nadir-viewing weighting functions calculated for two uniform relative humidity (RH) profiles at the six frequencies of the MIR: (a) RH = 30% and (b) RH = 100%. A temperature profile derived from the ECMWF product near the time and region of the aircraft flight was used in the calculations.

Figure 3. Profiles of (a) aerosol backscatter and (b) water vapor mixing ratio measured by the LASE over a portion of the region covered by L1. The dark pixels under the cloud patches A, B, and C, as well as a few other less conspicuous locations, in plot (a) indicate a total attenuation of LASE signals.

Figure 4. Variations of brightness temperatures observed by six frequency channels of the MIR over the same region shown in Figure 3. Notice that the 89 GHz channel is particularly sensitive to the presence of low-level liquid clouds.

Figure 5. Profiles of (a) aerosol backscatter and (b) water vapor mixing ratio for the line segments L2 and L3. The presence of intense cirrus clouds between the altitudes of 9-12 km totally attenuates the LASE signals below the cloud base.

Figure 6. Variations of brightness temperatures observed by six frequency channels of the MIR over the same region shown in Figure 5. The depressions of brightness temperatures from the five high-frequency channels in the region of cirrus clouds are highly frequency dependent.

Figure 7. Variations of (a) water vapor mixing ratio, (b) cloud liquid water, and (c) total precipitable water retrieved from the MIR measurements. Other relevant retrieval products are also included in plots (b) and (c).

Figure 8. A comparison of MIR-retrieved (open circles) and LASE-measured mixing ratio profiles (solid curves at four different times. Plots (a) and (c) are at the locations of clear sky, and (b) and (d), of cloudy sky.

Figure 9. A compariosn of the MIR-retrieved (solid curves) and LASE-measured (open circles) mixing ratios at five different altitudes, for the same period shown in Figure 7.

Figure 10. A comparison of the MIR-retrieved (solid curves) and LASE-measured (open circles) mixing ratios at five different altitudes for L2 and L3.

Figure 11. A comparison of the measured and retrieved values (both from LASE) of mixing ratio for L1.

Figure 12. A comparison of the LASE-retrieved and MIR-retrieved values of mixing ratio for L1, L2, and L3.

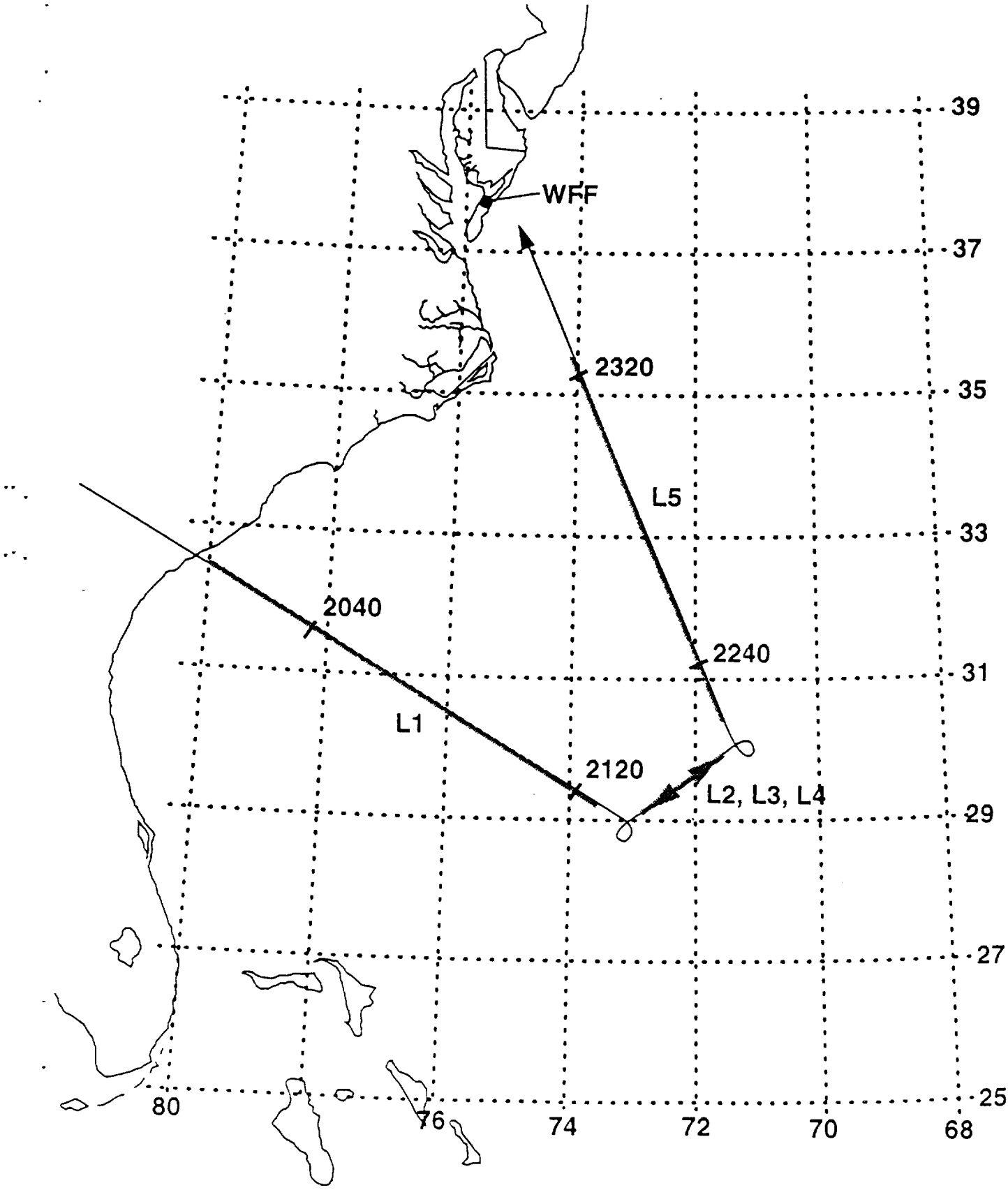

Figure 1

P965301

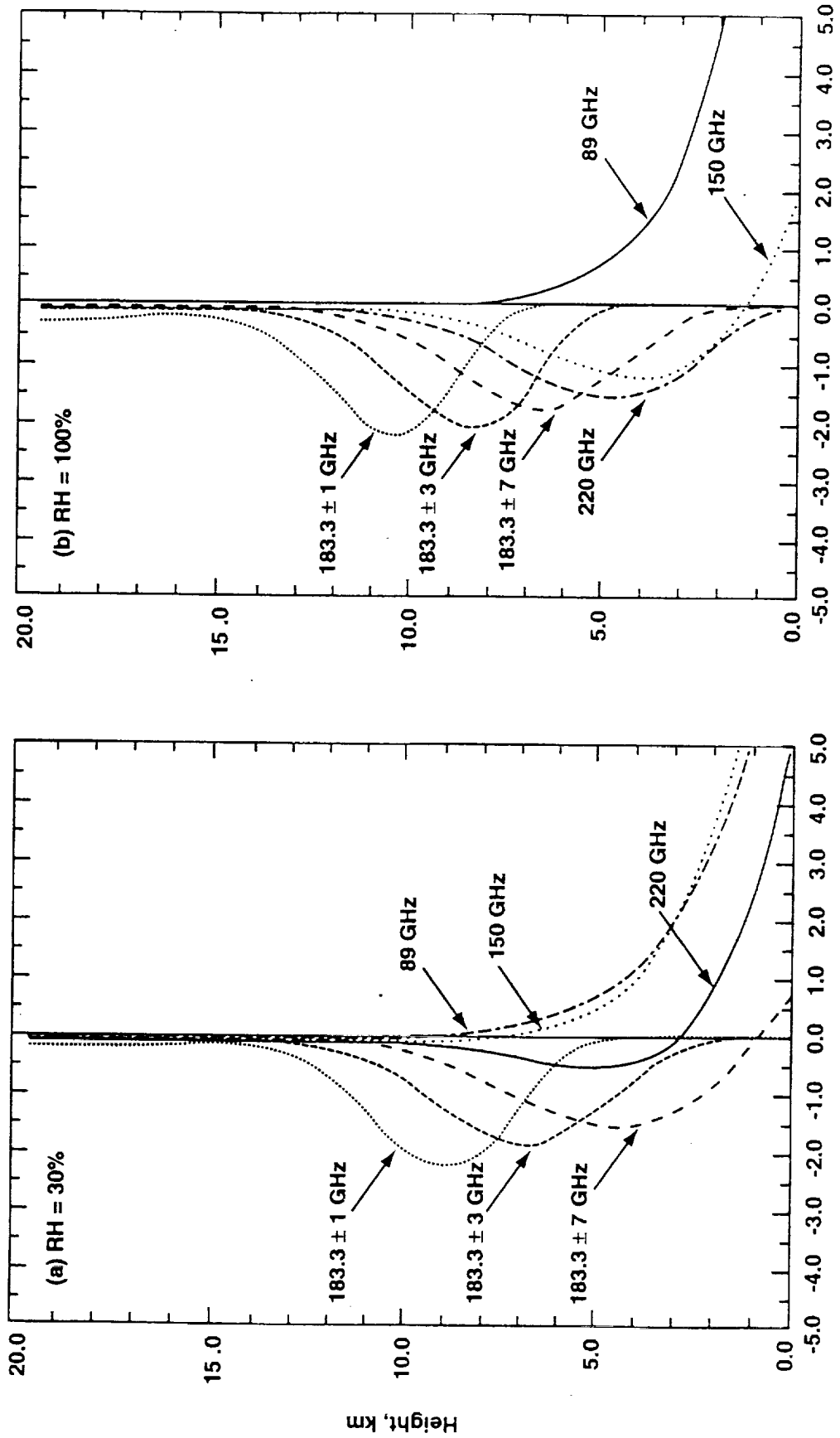
(a) RH = 30%
(b) RH = 100%
183.3 ± 1 GHz
183.3 ± 3 GHz
183.3 ± 7 GHz
89 GHz
150 GHz
220 GHz
Height, km
Nadir - Viewing Weighting Function, K/km
20.0
15.0
10.0
5.0
0.0
-5.0
-4.0
-3.0
-2.0
-1.0
0.0
1.0
2.0
3.0
4.0
5.0

Figure 2

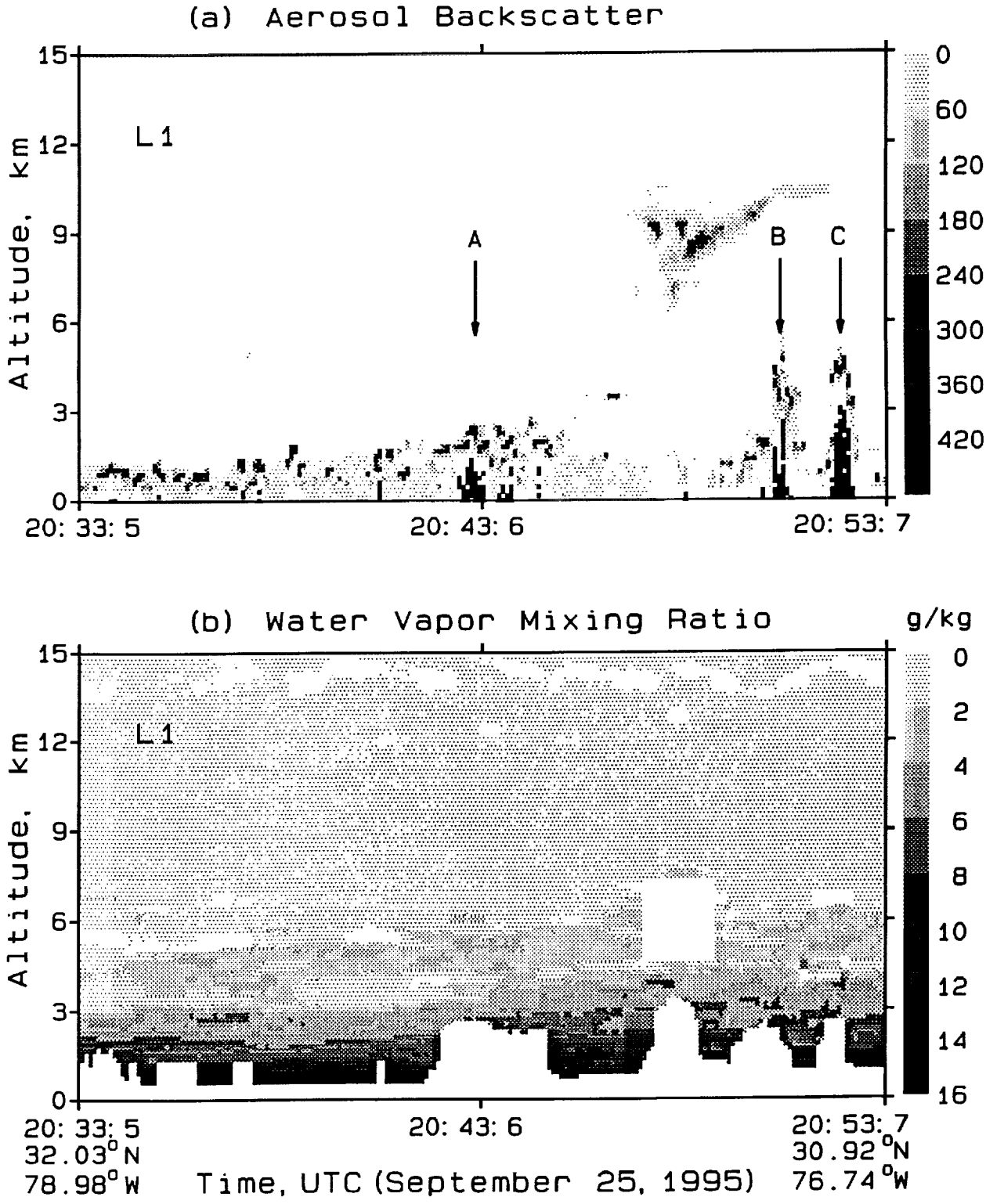
(a) Aerosol Backscatter
Altitude, km
15
12
9
6
3
0
L1
A
B
C
0
60
120
180
240
300
360
420
20: 33: 5
20: 43: 6
20: 53: 7
(b) Water Vapor Mixing Ratio
g/kg
0
2
4
6
8
10
12
14
16
20: 33: 5
32.03°N
78.98°W
20: 43: 6
20: 53: 7
30.92°N
76.74°W
Time, UTC (September 25, 1995)

Figure 3

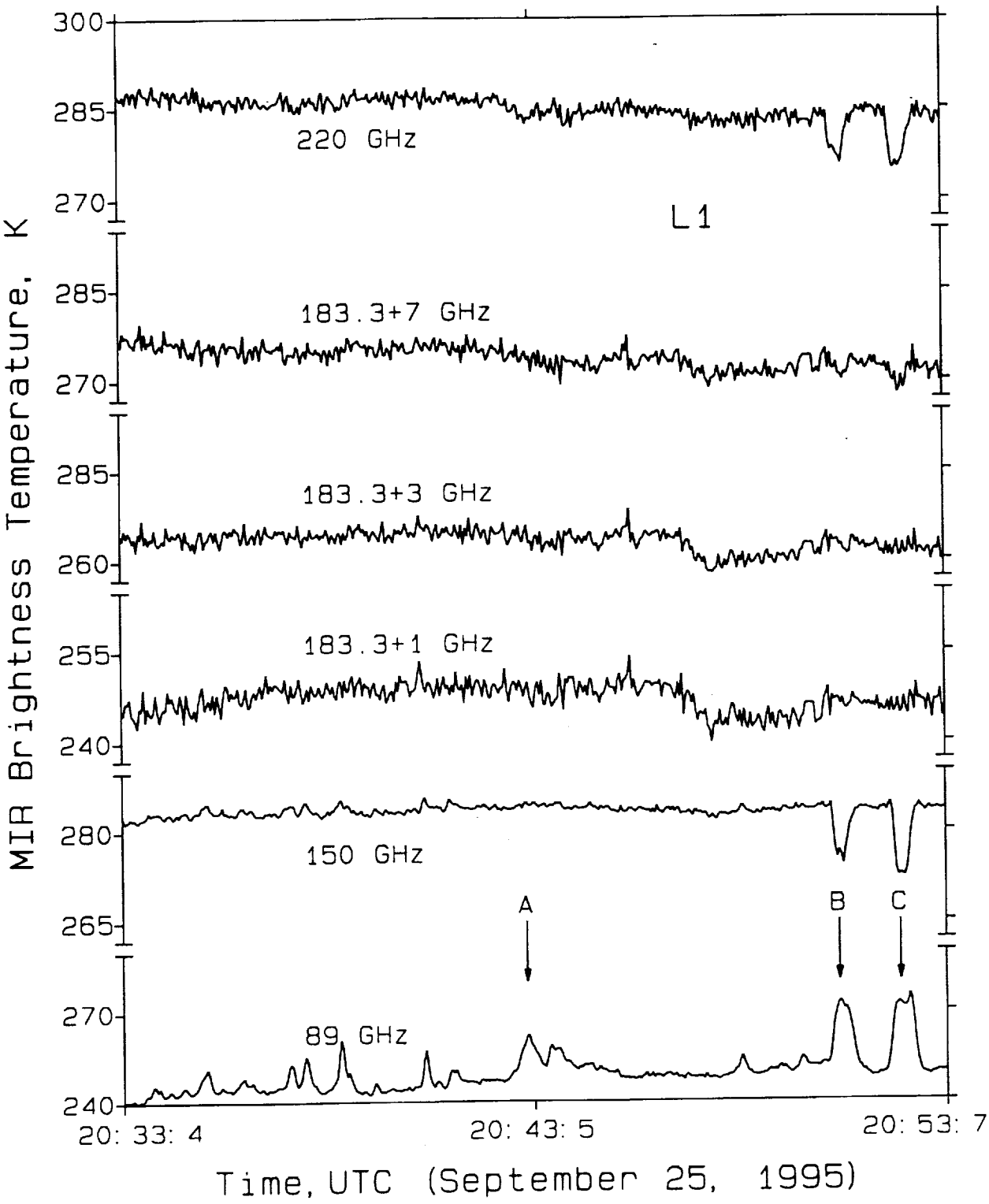
300
285
270
220 GHz
L1
285
270
183.3+7 GHz
285
260
183.3+3 GHz
255
240
183.3+1 GHz
280
265
150 GHz
A
B
C
270
240
89 GHz
MIR Brightness Temperature, K
20: 33: 4
20: 43: 5
20: 53: 7
Time, UTC (September 25, 1995)

Figure 4

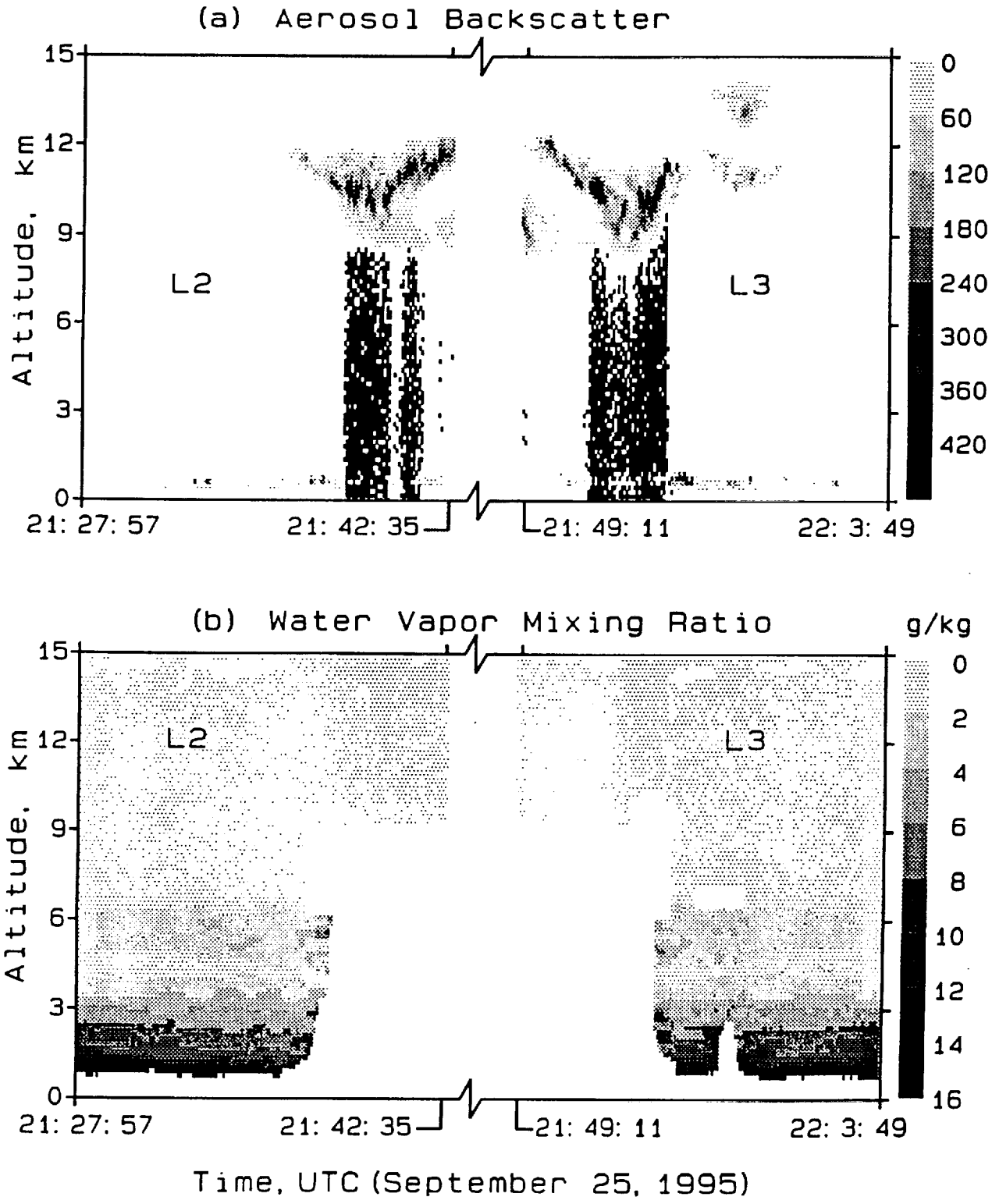
(a) Aerosol Backscatter
Altitude, km
15
12
9
6
3
0
L2
L3
0
60
120
180
240
300
360
420
21: 27: 57
21: 42: 35
21: 49: 11
22: 3: 49
(b) Water Vapor Mixing Ratio
g/kg
0
2
4
6
8
10
12
14
16
Time, UTC (September 25, 1995)

Figure 5

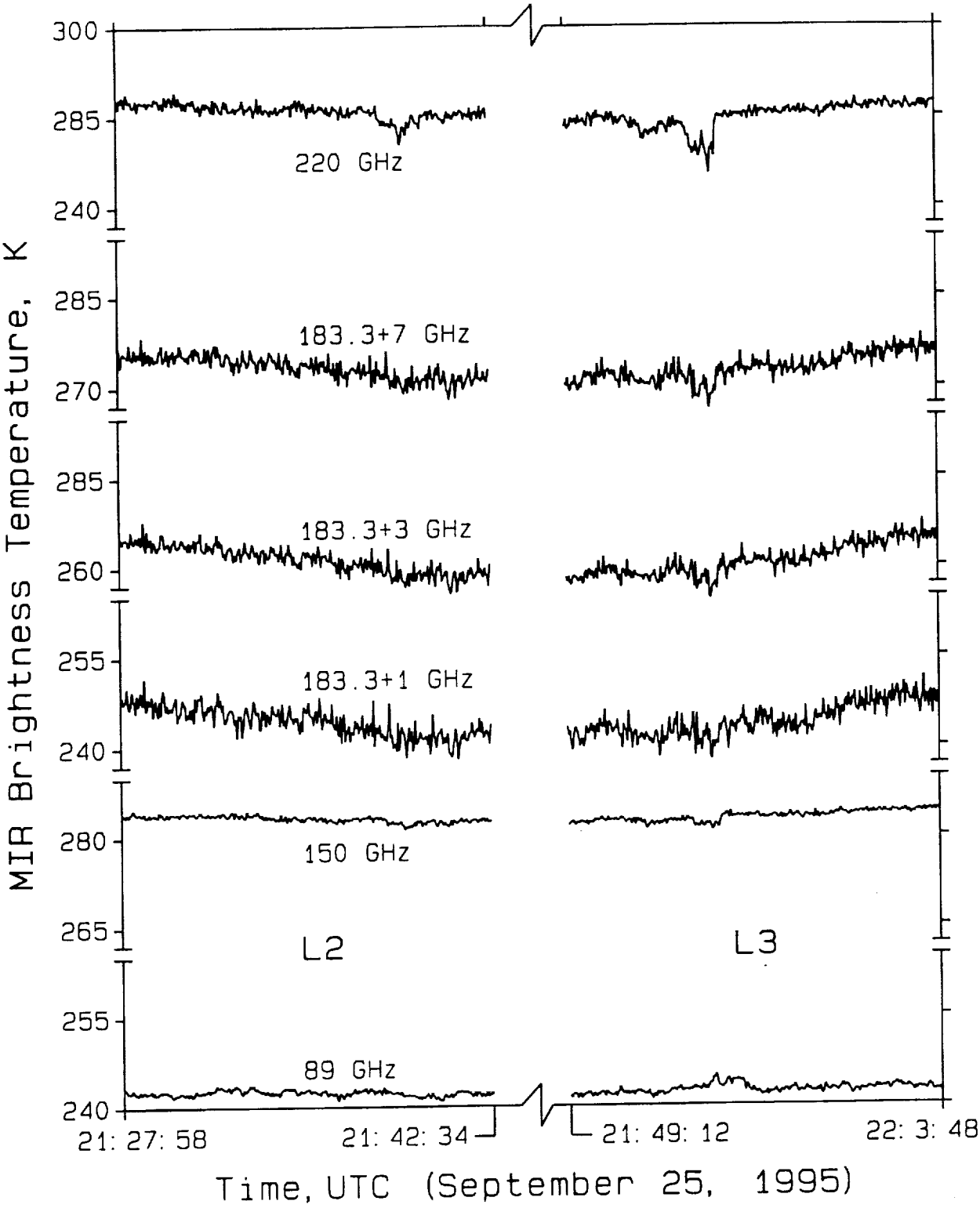
300
285
240
220 GHz
285
270
183.3+7 GHz
285
260
183.3+3 GHz
255
240
183.3+1 GHz
280
265
150 GHz
L2
L3
255
240
89 GHz
MIR Brightness Temperature, K
21: 27: 58
21: 42: 34
21: 49: 12
22: 3: 48
Time, UTC (September 25, 1995)

Figure 6

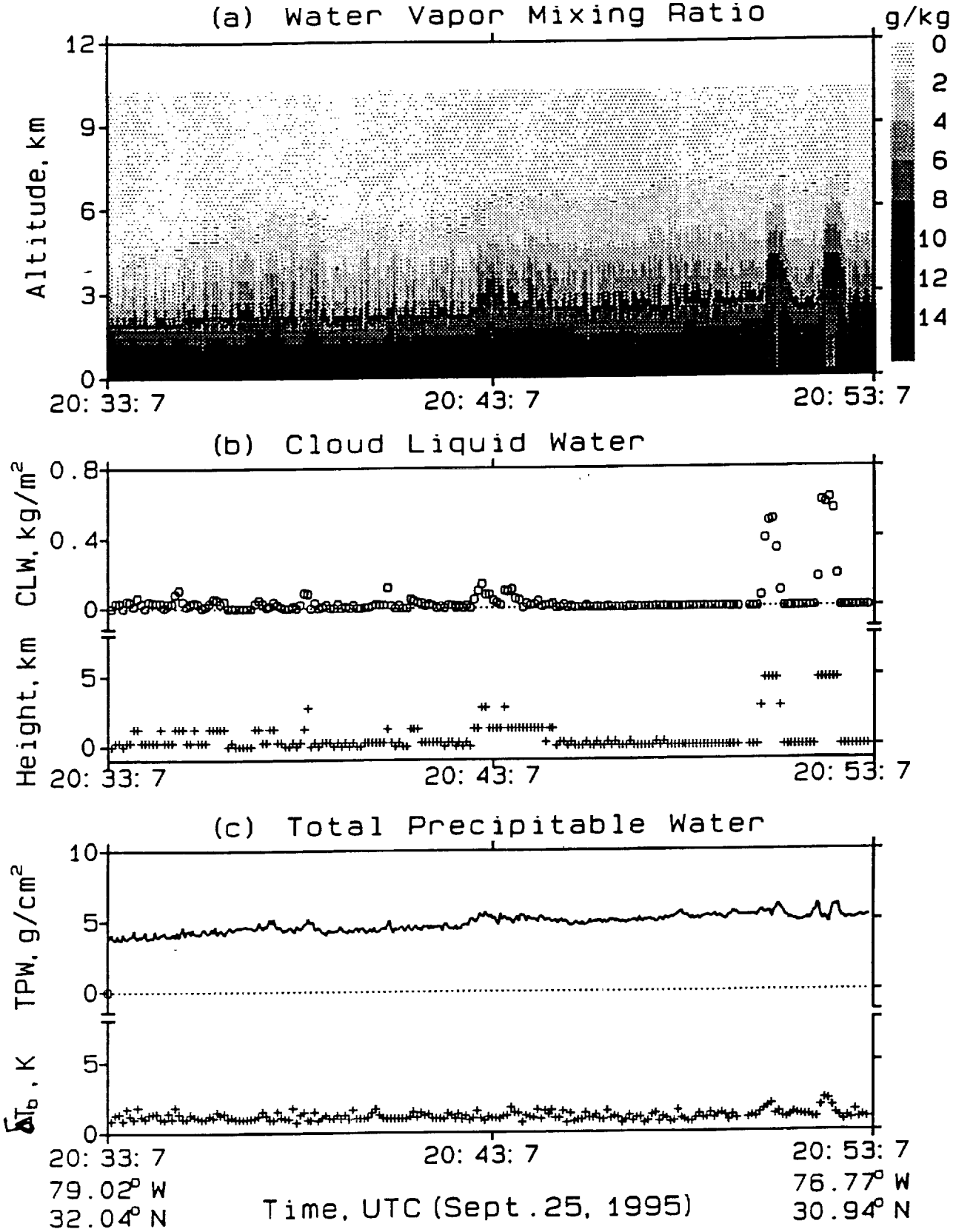
(a) Water Vapor Mixing Ratio
g/kg
0
2
4
6
8
10
12
14
Altitude, km
12
9
6
3
0
20: 33: 7
20: 43: 7
20: 53: 7
(b) Cloud Liquid Water
CLW, kg/m²
0.8
0.4
0
Height, km
5
0
20: 33: 7
20: 43: 7
20: 53: 7
(c) Total Precipitable Water
TPW, g/cm²
10
5
0
ΔTb, K
5
0
20: 33: 7
79.02° W
32.04° N
20: 43: 7
Time, UTC (Sept. 25, 1995)
20: 53: 7
76.77° W
30.94° N

Figure 7

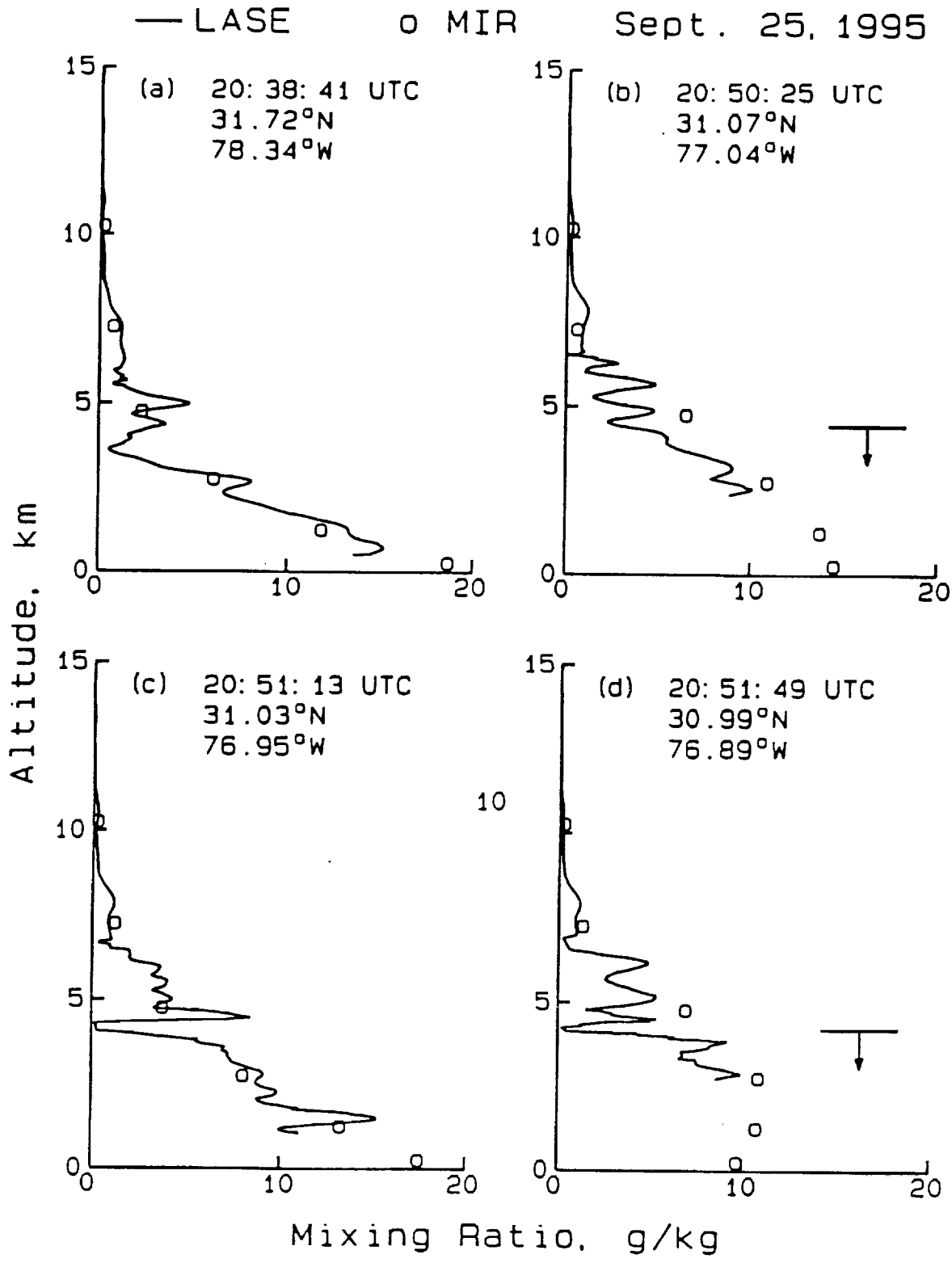
— LASE o MIR Sept. 25, 1995
(a) 20: 38: 41 UTC
31.72°N
78.34°W
(b) 20: 50: 25 UTC
31.07°N
77.04°W
(c) 20: 51: 13 UTC
31.03°N
76.95°W
(d) 20: 51: 49 UTC
30.99°N
76.89°W
Altitude, km
Mixing Ratio, g/kg

Figure 8

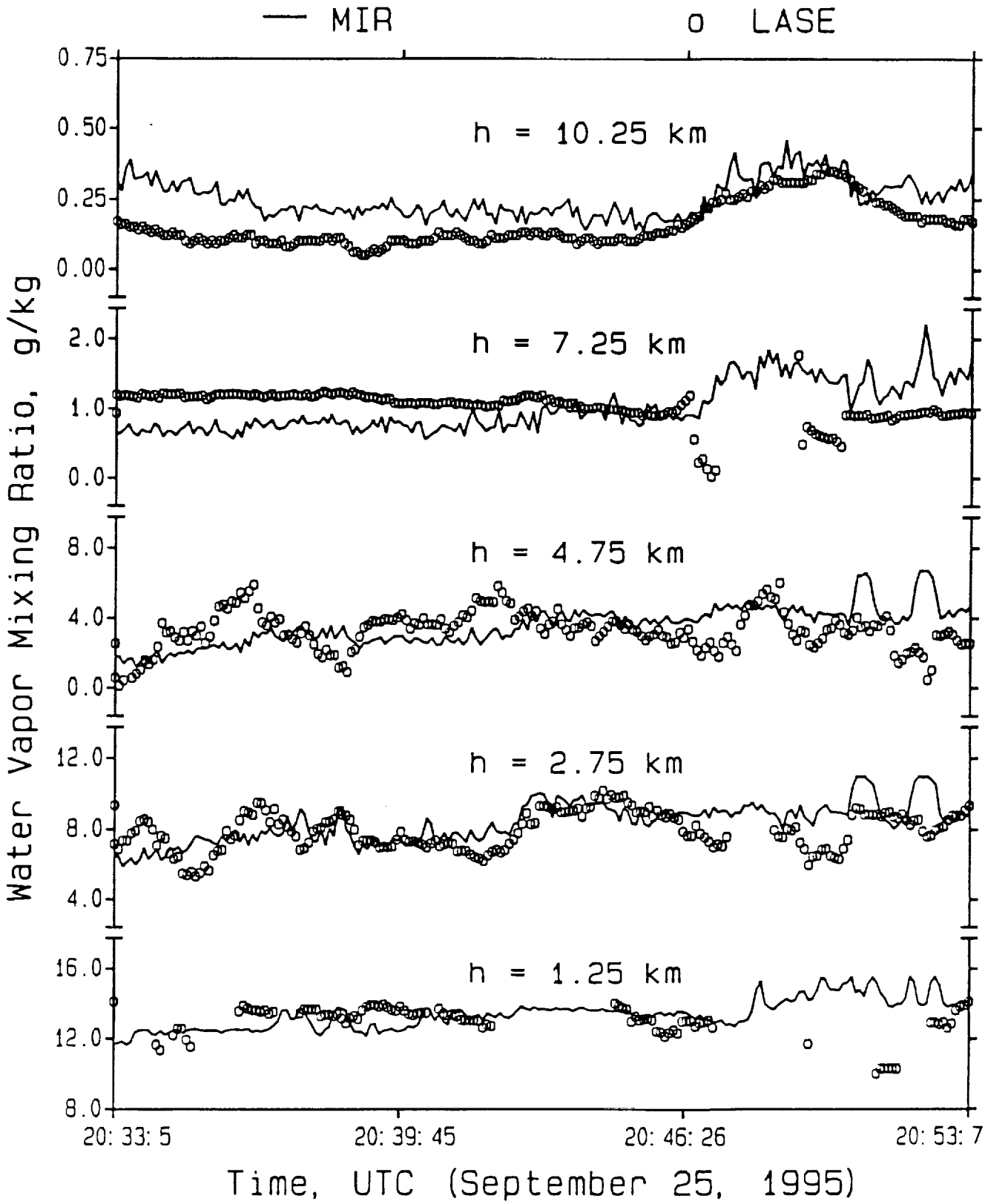
— MIR
o LASE
h = 10.25 km
h = 7.25 km
h = 4.75 km
h = 2.75 km
h = 1.25 km
0.75
0.50
0.25
0.00
2.0
1.0
0.0
8.0
4.0
0.0
12.0
8.0
4.0
16.0
12.0
8.0
Water Vapor Mixing Ratio, g/kg
20: 33: 5
20: 39: 45
20: 46: 26
20: 53: 7
Time, UTC (September 25, 1995)

Figure 9

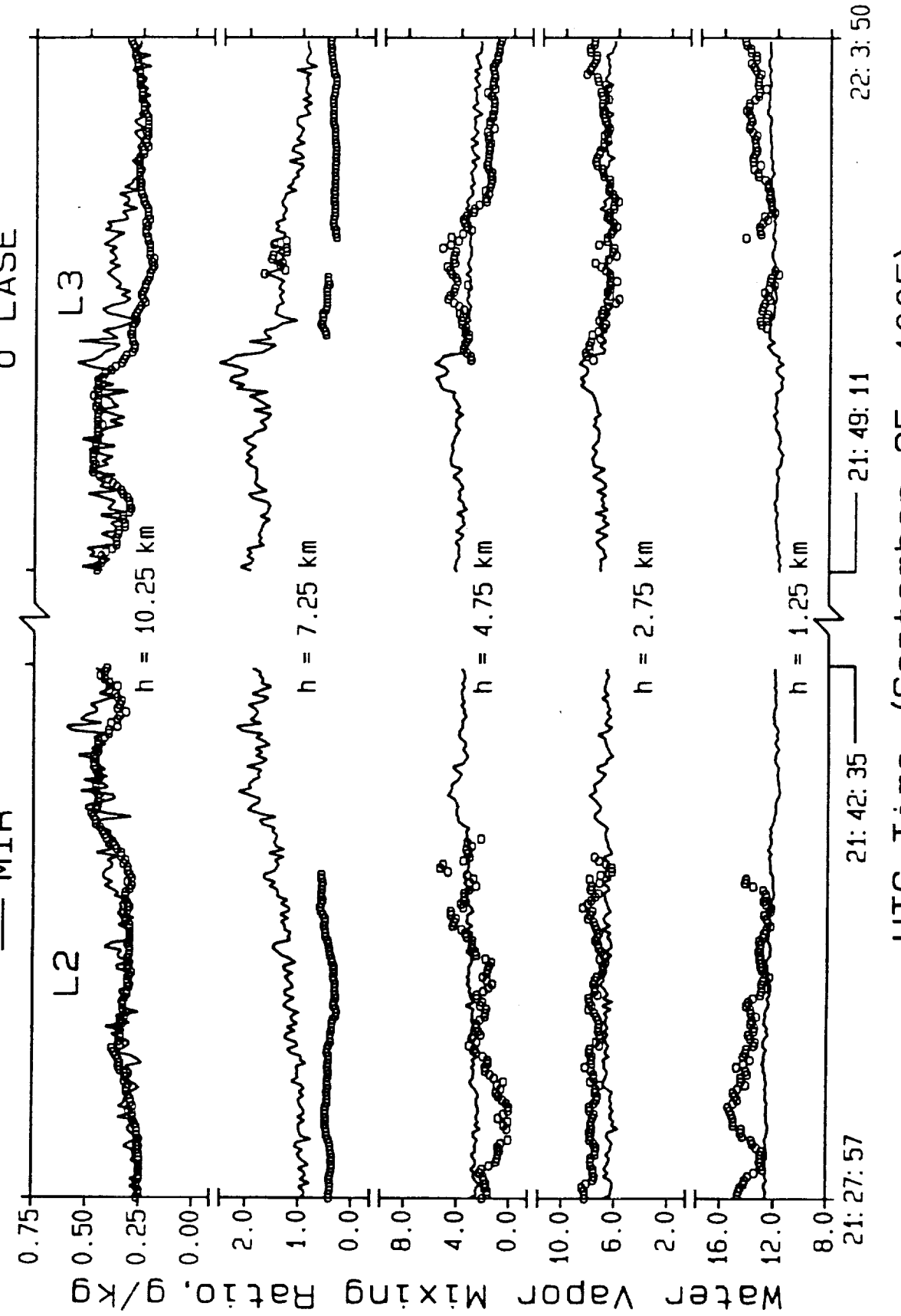
— MIR
o LASE
L2
L3
h = 10.25 km
h = 7.25 km
h = 4.75 km
h = 2.75 km
h = 1.25 km
0.75
0.50
0.25
0.00
2.0
1.0
0.0
8.0
4.0
0.0
10.0
6.0
2.0
16.0
12.0
8.0
21: 27: 57
21: 42: 35
21: 49: 11
22: 3: 50
UTC Time (September 25, 1005)
Water Vapor Mixing Ratio, g/kg

Figure 10

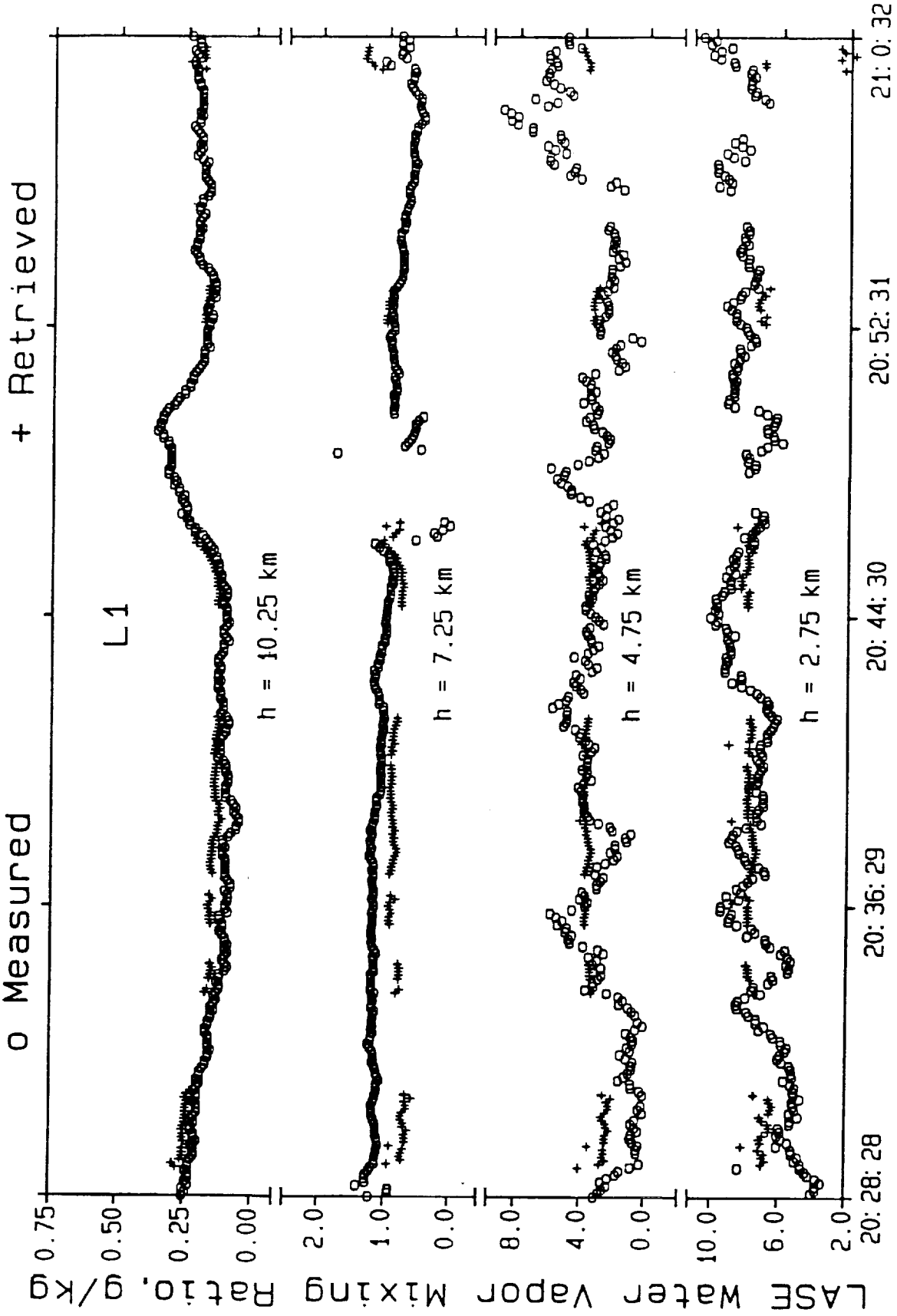
o Measured
+ Retrieved
L1
h = 10.25 km
h = 7.25 km
h = 4.75 km
h = 2.75 km
LASE Water Vapor Mixing Ratio, g/kg
0.75
0.50
0.25
0.00
2.0
1.0
0.0
8.0
4.0
0.0
10.0
6.0
2.0
20: 28: 28
20: 36: 29
20: 44: 30
20: 52: 31
21: 0: 32
UTC Time (September 25, 1995)

Figure 11

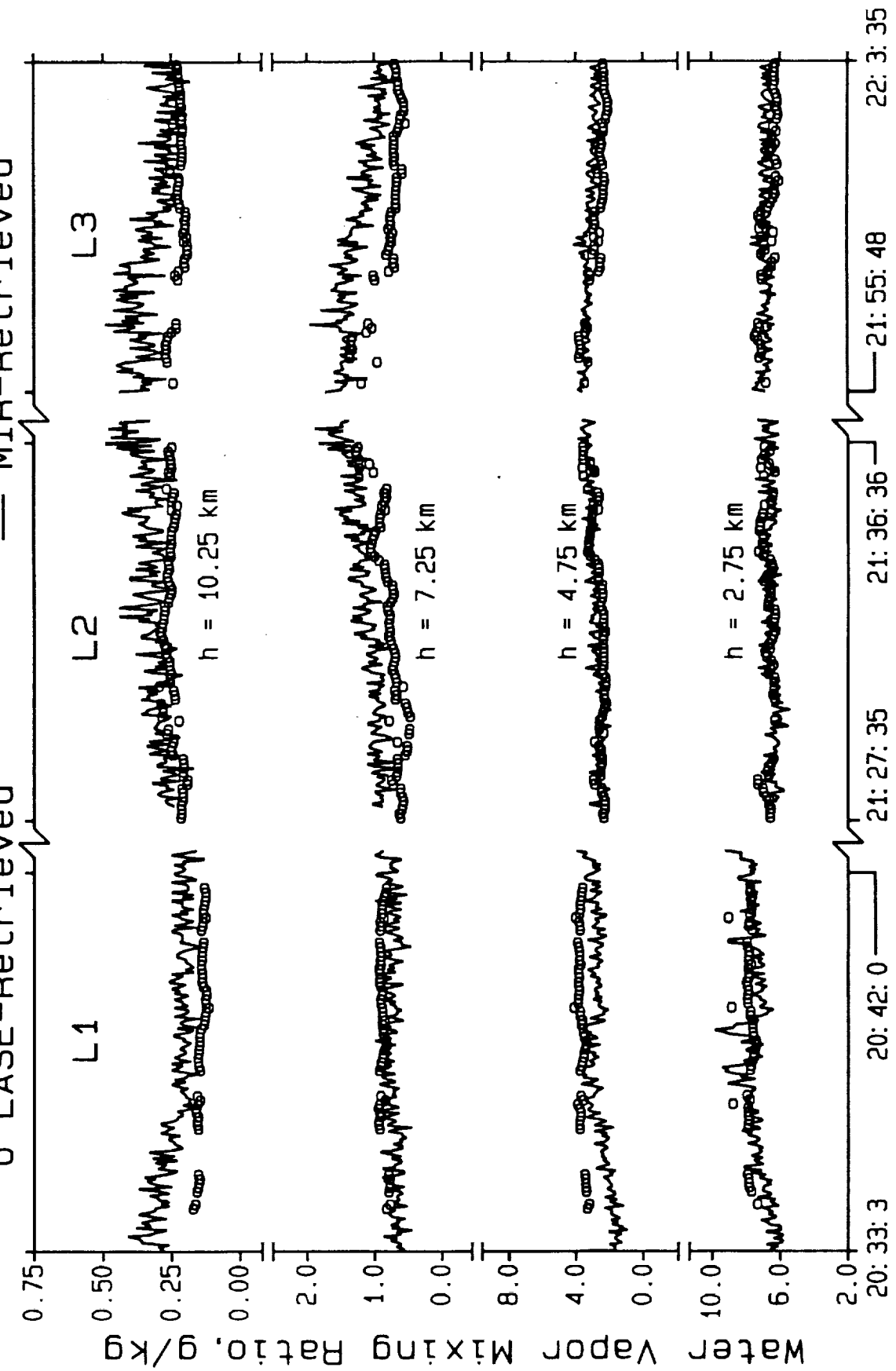
o LASE-Retrieved
— MIR-Retrieved
L1
L2
L3
h = 10.25 km
h = 7.25 km
h = 4.75 km
h = 2.75 km
Water Vapor Mixing Ratio, g/kg
0.75
0.50
0.25
0.00
2.0
1.0
0.0
8.0
4.0
0.0
10.0
6.0
2.0
20: 33: 3
20: 42: 0
21: 27: 35
21: 36: 36
21: 55: 48
22: 3: 35
UTC Time (September 25, 1995)

Figure 12